ACS Catalysis

Research Article

pubs.acs.org/acscatalysis

Platinum–Ruthenium Heterogeneous Catalytic Anodes Prepared by Atomic Layer Deposition for Use in Direct Methanol Solid Oxide Fuel Cells

Heon Jae Jeong,[†] Jun Woo Kim,[†] Kiho Bae,[†,‡] Hojean Jung,[†] and Joon Hyung Shim*[,†]

[†]School of Mechanical Engineering, Korea University, 145 Anam-ro, Seongbuk-gu, Seoul 136-713, South Korea

[‡]High-Temperature Energy Materials Research Center, Korea Institute of Science and Technology (KIST), Hwarangno 14-gil, 5, Seongbuk-gu, Seoul 136-791, South Korea

Supporting Information

ABSTRACT: Heterogeneous Pt–Ru catalysts are synthesized by atomic layer deposition (ALD) of Ru onto a porous Pt mesh and employed as the anode in direct methanol solid oxide fuel cells (DMSOFCs). The degree of Ru coverage is controlled by the number of deposition cycles employed in catalyst preparation; samples are prepared using 50, 100, 200, 300, and 400 cycles. The dispersed nature of the ALD Ru coating is confirmed by auger electron spectroscopy and high-resolution transmission electron microscopy. DMSOFC performance is measured at several temperatures between 300 and 450 °C. Optimal ALD Ru coverage results in DMSOFC power and electrode impedance values close to ones from SOFCs with Pt electrodes running on hydrogen. Thermal stability is also improved significantly, preventing agglomeration of the Pt mesh. X-ray photoelectron spectroscopy is used to analyze the chemical properties of the surface and confirms that increased ALD Ru coverage results in a dramatic reduction in the amount of surface-bound carbon monoxide (CO) present after cell operation. This suggests that improved anode kinetics resulted from the reduction of the CO-passivated Pt layer.

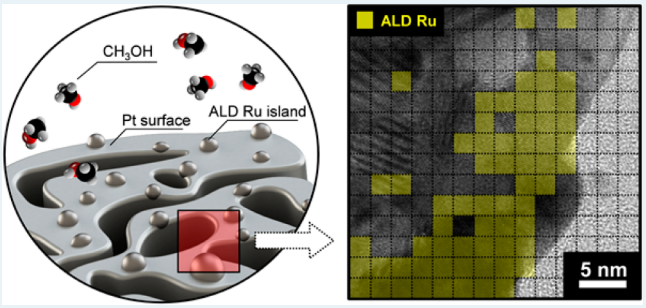

KEYWORDS: *heterogeneous catalysts, atomic layer deposition, direct methanol solid oxide fuel cell, platinum, ruthenium*

1. INTRODUCTION

Methanol has attracted considerable attention in the fuel cell industry as an alternative to hydrogen for several reasons.[1−5] First, methanol is a stable liquid, making it easy to transport and store. In addition, methanol has a relatively high volumetric energy density compared to other liquid hydrocarbon fuels. Finally, methanol can be injected directly into fuel cell stacks without the need for a fuel reformer or sulfur removal, which are generally both necessary for hydrogen-based fuel cells.

High-performance methanol fuel cells require high-performance anodic catalysts to effect methanol oxidation.[5,6] Currently, Pt/Ru bimetallic catalysts are the most promising because of the rapid oxidation of methanol on the Pt surface combined with the Ru-catalyzed oxidation of carbon monoxide (CO) to carbon dioxide (CO_2).[7−11] A variety of methods have been investigated for the preparation of these catalysts, including impregnation and techniques relying on colloidal dispersions and microemulsions.[11−16] In addition, atomic layer deposition (ALD) has recently attracted attention as an alternative method. ALD, a modified chemical vapor deposition technique, uses gaseous precursors as material sources for film synthesis. In this process, films grow via a self-limiting thermal reaction between the evaporated source chemicals and the heated substrate; as long as sufficient material is present on the substrate surface, the growth rate is independent of gas concentration and flow direction.[17−20] For this reason, ALD films can grow uniformly along uneven substrate surfaces, enabling catalytic materials to be evenly dispersed over materials with high surface areas, such as nanoscale spheres, trenches, and rods, as well as the inner surfaces of nanoporous materials.[21−30]

ALD has been repeatedly employed to develop metallic catalysts for methanol oxidation.[25−27] Christensen and co-workers demonstrated that aluminum oxide nanoparticles coated with Pt and Ru by ALD outperform a mixture of the corresponding pure metallic particles.[25] In addition, highly dispersed Pd particles uniformly deposited by ALD along the inner surfaces of porous silica showed effective methanol oxidation.[26,27] However, although the authors emphasized that the main application of their findings would be in the development of catalysts for direct methanol fuel cells (DMFCs), none of these studies integrated these materials into working fuel cells. Although ALD Pt catalysts have been shown to be effective catalysts in this regard,[23,24,30−32] there are no reports on ALD Ru catalysts.

Received: December 19, 2014
Revised: February 6, 2015
Published: February 6, 2015

DOI: 10.1021/cs502041d
ACS Catal. 2015, 5, 1914−1921

In this study, we prepared Pt mesh coated with Ru shell by ALD and tested the potential of this material as an anodic catalyst in a direct methanol solid oxide fuel cell (DMSOFC) utilizing a ceramic electrolyte fabricated from gadolinium-doped ceria (GDC). In the search for optimal content of Ru in terms of electrochemical performance, the ALD Ru was introduced to the Pt surface over 50, 100, 200, 300, and 400 cycles; these samples are referred to as Pt/Ru ALD 50, Pt/Ru ALD 100, Pt/Ru ALD 200, Pt/Ru ALD 300, and Pt/Ru ALD 400, respectively, whereas samples that were not coated with Ru are simply referred to as Pt. A schematic of our work is shown in Figure 1. Previous work has described the ALD Ru

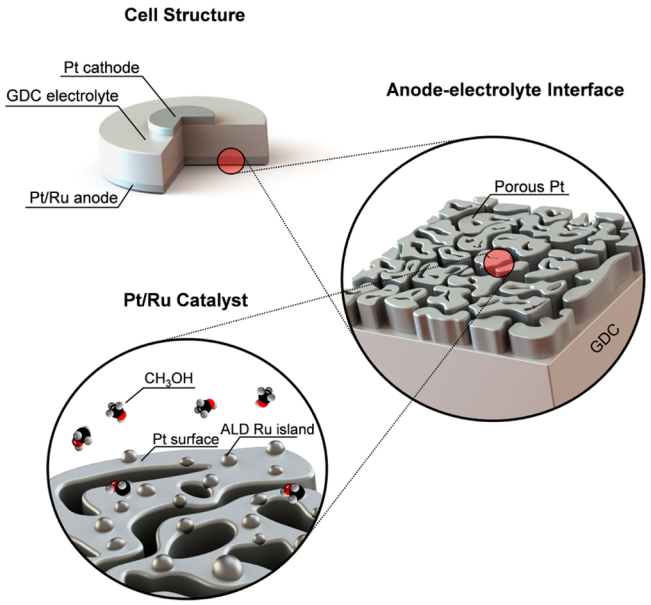

Figure 1. Schematic of a GDC-based SOFC with porous Pt/Ru ALD anodes.

reaction mechanism, which proceeds via the complete oxidation of the metallic Ru precursor adsorbed on either Pt or Ru. This process can be represented by the following reactions, representing a single pulse cycle in the process; bis(ethylcyclopentadienyl) ruthenium(II) ($Ru(EtCp)_2$) is used as the Ru precursor.[33]

Ru precursor pulse cycle:

$$Ru(C_5H_4C_2H_5)_{2(g)} + 37O_{(ads)} \rightarrow Ru_{(s)} + 14CO_{2(g)} + 9H_2O_{(g)} \quad (1)$$

Oxygen pulse cycle:

$$18.5O_{2(g)} \rightarrow 37O_{(ads)} \quad (2)$$

A structure consisting of a Pt core with a Ru shell has been reported as the most effective in terms of both catalytic performance and stability.[34,35] The performance of the developed electrodes was then evaluated with respect to surface kinetic impedance and fuel cell power output. In addition, the thermal and chemical stability of the catalyst was investigated by studying the morphology and chemical composition of the material both before and after cell operation.

2. EXPERIMENTAL SECTION

2.1. Preparation of GDC Electrolyte Support. GDC pellets were synthesized by uniaxial pressing of commercial GDC powder (Rhodia) at approximately 1600 kgf cm^{-2}, followed by sintering at 1450 °C for 10 h in air. The thickness of the pellets after polishing was about 350 μm, and the diameter was 1 cm. The uniform density of the synthesized pellets was confirmed by field emission scanning electron microscopy (FESEM, S-4800, Hitachi, Korea University) and compaction curve analysis. The polycrystalline nature of the samples was confirmed by X-ray diffraction (XRD, D/MAX-2500 V/PC, Rigaku, Korea University), as shown in Figure S1a. Impedance measurements with porous Pt electrodes in fuel cell operation with methanol confirmed that the ionic conductivity of the samples was in agreement with published reference values, as shown in Figure S1b.[36,37]

2.2. Sputtering of Pt Electrodes. The porous Pt electrodes were prepared by DC sputter deposition, applied to both sides of the GDC pellet. The cathode was deposited using a sputter mask with a diameter of 0.35 cm. The procedure was conducted at 100 W in a 90 mTorr Ar atmosphere, which was set after an initial evacuation to 10^{-3} mTorr. Sputtering for 10 min gave a porous Pt mesh with a thickness of 150 nm.

2.3. ALD of Ru. Ru ALD was achieved using $Ru(EtCp)_2$ (UP Chemical) and pure oxygen (99.9%) as the precursor and oxidant, respectively, whereas a thermal ALD chamber (ICOT Company Inc.) was employed for the procedure; structural details of the ALD system are given in previous publications,[38,39] and optimal conditions for metallic Ru fabrication are summarized in the literature.[33,40,41] The substrate temperature was set to 320 °C, while the precursor and oxidant were supplied in 5 s pulses using pure nitrogen (99.99%) as a carrier gas, set to a flow rate of 1 sccm. The reaction chamber was purged with nitrogen between the precursor and oxidant pulses at the same flow rate. To confirm the growth rate of ALD Ru, we have put 1 cm by 1 cm Si (100) pieces beside the fuel cell sample and have measured the cross-sectional film thickness using FESEM, as shown in Figure S2a. As a result, we have confirmed that the Ru films grow in the ALD mode where thickness of the film grown per one precursor pulsing cycle saturates regardless of varied pulsing time as shown in Figure S2b. The resulting growth rate was found to be 0.4–0.5 Å $cycle^{-1}$, which is in good agreement with reference values.[33,40,41] The dispersion pattern of the deposited Ru was identified by auger electron spectroscopy (AES, PHI 700Xi, ULVAC-PHI, Hanyang University). High-resolution transmission electron microscopy (HRTEM, JEM-2100F, JEOL, Hanyang University) with the energy-dispersive X-ray spectroscopy (EDS) composition analysis was used to probe the Ru nanomorphology. The chemical composition of the surfaces was analyzed by X-ray photoelectron spectroscopy (XPS, PHI 5000 VersaProbe, ULVAC-PHI, Korea Institute of Science and Technology).

2.4. Electrochemical Characterization and Fuel Cell Measurement. Cell performance was measured by current–voltage (I–V) analysis and AC impedance spectroscopy at four specific temperatures between 300–450 °C. Electrochemical impedance spectroscopy (EIS) was measured with a potentiostat (Reference 3000, Gamry Instruments) and was conducted over a frequency range of 10^6–1 Hz and with a voltage amplitude of 10 mV. The anode side of the fuel cell was sealed to a small chamber by means of a gold gasket, while the nitrogen carrier gas was bubbled through pure liquid methanol (99.9%) at a flow rate of 20 sccm at room temperature. The cathode side was exposed to atmosphere. The details of customized fuel cell measurement setup are shown in Figure S3. As shown in Figure S3a, reactants such as the methanol/nitrogen mixture fuel were introduced into anode chamber side, and

DOI: 10.1021/cs502041d
ACS Catal. 2015, 5, 1914–1921

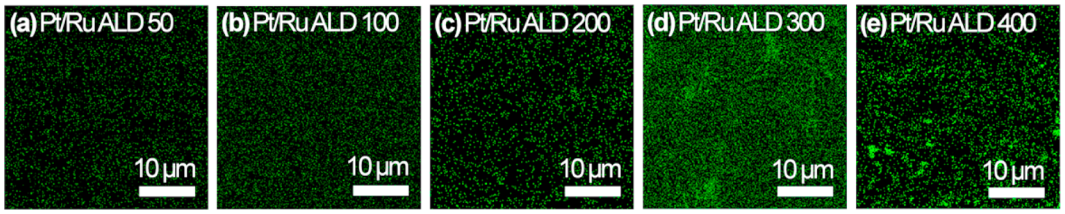

Figure 2. AES composition mapping of ALD Ru on sputtered Pt mesh. (a) Pt/Ru ALD 50, (b) Pt/Ru ALD 100, (c) Pt/Ru ALD 200, (d) Pt/Ru ALD 300, and (e) Pt/Ru ALD 400. Ru deposits are shown in green.

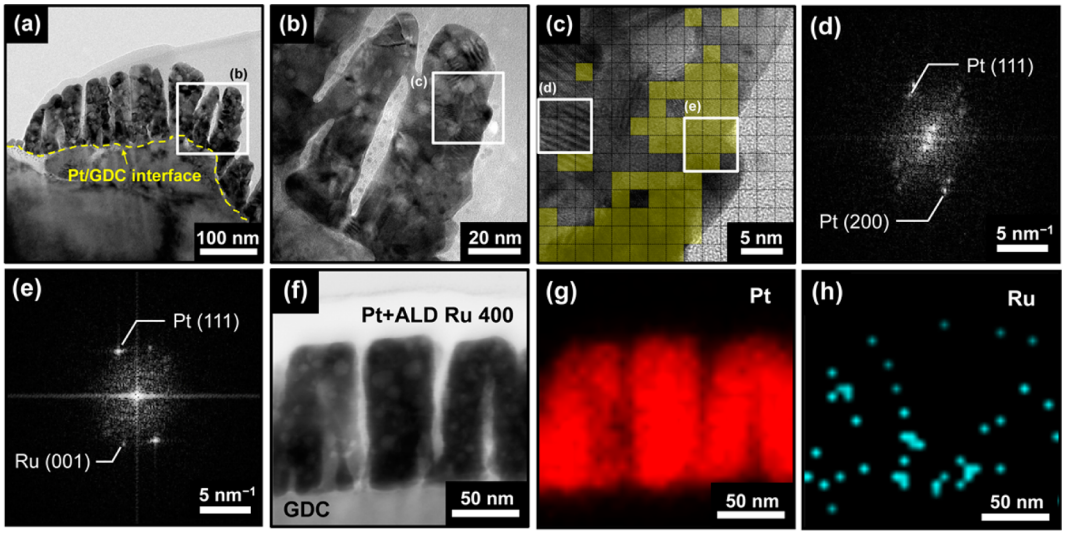

Figure 3. (a)−(c) HRTEM cross-sectional images of a Pt/Ru ALD 400 anode surface showing the presence of sputtered Pt columns. In (c), the presence of deposited Ru is indicated in yellow. (d) and (e) show the corresponding diffraction patterns for Pt and Ru at the points marked in (c). (f)−(h) HRTEM cross-sectional image of the Pt/Ru ALD 400 anode surface with the EDS composition analysis.

products such as H_2O, CO_2, and other intermediates were emitted to a ventilating opening. As shown in Figure S3b, we can precisely control inlet gas flow rate from 0 to 200 sccm by using the mass flow rate controller, and we can control the chamber temperature from room temperature to 1000 °C by using the temperature controller. For a fuel cell measurement, the probe tip contact method was used as shown in Figure S3c. Our customized fuel cell chamber was installed on the button cell heater linked with the temperature controller. The Pt probe tip was used as the working electrode, and the counter electrode was connected to anode chamber side. Pure nitrogen gas was used as carrier gas to bubble pure methanol, as shown in Figure S3d.

3. RESULTS AND DISCUSSION

3.1. Morphological and Compositional Analysis of Pt/Ru ALD Surface. Figure 2 shows the AES images of the catalyst samples; green points represent ALD Ru. Overall, ALD Ru did not fully cover the entire Pt surface, even after 400 cycles; the total Ru surface coverage peaked at 20.7% at this point, with Ru accumulating inconsistently in concentrated pockets. This pattern was also observed with HRTEM, as shown in Figure 3. The HRTEM cross-sectional images further reveal that the ALD Ru film formed as islands along the surface of the Pt columns. To further investigate the growth mode of the ALD Ru, we have prepared another set of samples with ALD Ru (50−400 cycles) deposited on a mesh grid coated with porous Pt sputtered through the same process with one for our fuel cell samples. HRTEM images of the ALD Ru on the mesh also confirmed the island nucleation of Ru on Pt, as shown in Figure S5. The details of the grid-ALD Ru experiment are described in the Supporting Information. This island growth of the ALD Ru can be explained by the lack of appropriate surface functional groups on the Pt substrate, which are essential to Ru chemisorption and, consequently, film growth.[42−44] Ru also has a much higher surface energy of 3.9 J m^{-2}, compared to 2.7 J m^{-2} for Pt; the potential decrease in surface energy would favor decreased Ru surface area through the formation of Ru clusters.[42,45] This growth pattern has been heavily reported for the deposition of materials with low surface energy on surfaces lacking suitable functional groups,[46−48] and has been adequately rationalized by the Markov nucleation model.[49,50]

3.2. Fuel Cell Performance. Figure 4a shows I−V and power output data for Pt, Pt/Ru ALD 50, Pt/Ru ALD 100, and Pt/Ru ALD 200 cells tested at 400 °C, whereas Figure 4b shows maximum power density. All bimetallic catalysts outperform pure Pt, confirming that ALD treatment enhances surface kinetics. Overall, the Pt/Ru ALD 100 cell provided the highest power output, with an increase in performance of more than 1 order of magnitude over the pure Pt cell for all measurement temperatures. For comparison, the same cell configuration was evaluated for pure Pt with dry hydrogen; enhancement of the maximum power density of the control, when compared to the Pt/Ru ALD 100 cell, was less than 40% for all temperatures except 450 °C, where it was 63%, as shown in Figure 4c.

EIS was conducted to investigate impedance of the electrode processes. Figure 5a shows EIS spectra of a Pt/Ru ALD 100 cell characterized at 400 °C under different bias conditions; this

DOI: 10.1021/cs502041d
ACS Catal. 2015, 5, 1914−1921

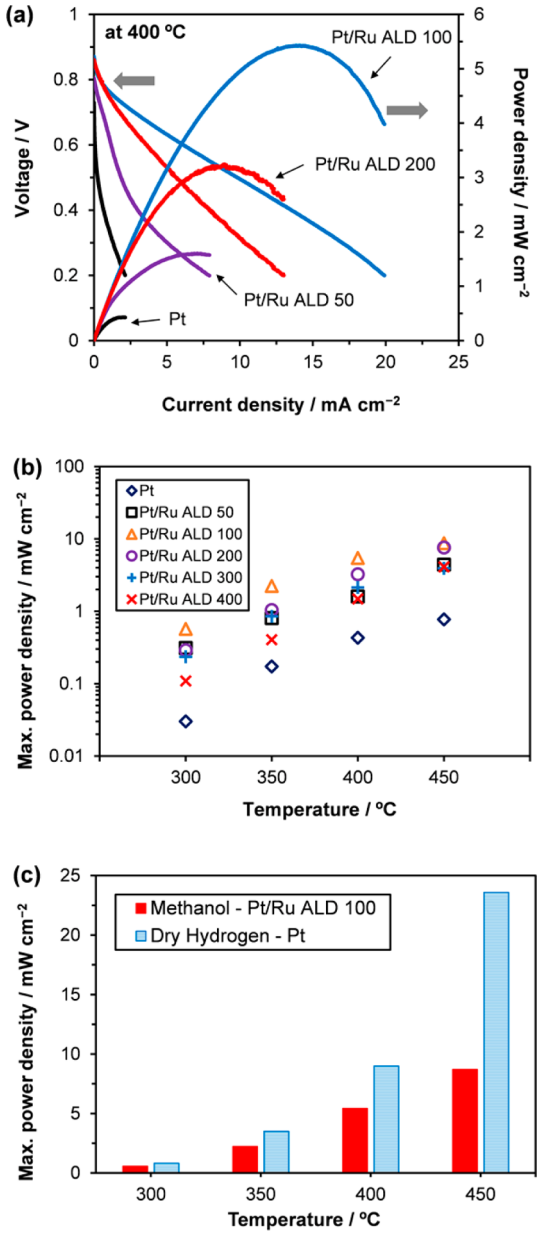

Figure 4. (a) Fuel cell performance at 400 °C for Pt, Pt/Ru ALD 50, Pt/Ru ALD 100, and Pt/Ru ALD 200. (b) Maximum power densities for Pt, Pt/Ru ALD 50, Pt/Ru ALD 100, Pt/Ru ALD 200, Pt/Ru ALD 300, and Pt/Ru ALD 400 running with methanol, alongside a Pt cell running with dry hydrogen. (c) Comparison of maximum power densities from the Pt/Ru ALD 100 cell running with methanol and the Pt cell running with dry hydrogen.

technique has been previously applied to distinguish impedance contributions from charge transport and electrochemical processes.[51,52] Generally, high frequency arcs represent electrolyte resistance, whereas low frequency arcs represent electrode or polarization impedance; the fact that impedance values obtained from fitting to the arcs appeared at high frequencies showed no apparent change to applied bias voltage as shown in Figure 5b, but impedance from the low frequency arc significantly decreased with increased overpotential, as shown in Figure 5c, confirms that this is the case for these data.

Given these results, electrolyte and electrode impedances were compared for the various Pt/Ru ALD DMSOFCs with respect to area-specific resistance (ASR), using a cell voltage of 0.7 V and a temperature of 400 °C. Overall, electrode impedances were significantly greater than electrolyte impedances, implying that overall performance is governed by an electrode process. The electrode ASR of the Pt/Ru ALD 100 cell was lowest (41 Ω cm^2), whereas that of the pure Pt sample was more than 2 orders of magnitude higher (5330 Ω cm^2); this explains the superior performance of the Pt/Ru ALD 100 cell.

3.3. Thermal Stabilization Effect of ALD Ru. To investigate the cause of the large electrode impedance measured in the Pt cell, changes in morphology resulting from cell operation were analyzed through FESEM. The Pt columns in all samples were initially separated, as shown in Figure 6. After the 450 °C cell test, severe morphological changes were observed in the Pt cell, where most of the Pt aggregated into clusters that contained only small spaces.

The triple-phase boundary (TPB) is the area where the electrolyte, electrode, and gas phase are in physical contact; it is here that the majority of charge transfer and methanol oxidation takes place. Image processing software calculated the TPB density of the Pt cell to be 0.020 nm^{-1} initially, which is consistent with previous reports.[53] However, that value dropped to 0.005 nm^{-1} after electrochemical testing, which is consistent with previous reports on thermal aggregation of sputtered porous Pt, a phenomenon that is especially common after SOFC testing.[53−55] However, ALD Ru surface treatment significantly reduced thermal coarsening, as shown in Figure 6. The Pt/Ru ALD 100 sample demonstrates this quantitatively, with TPB densities of 0.015 nm^{-1} and 0.012 nm^{-1} before and after cell testing, respectively. The effect for the Pt/Ru ALD 200 sample was even more significant, with a change of only 0.001 nm^{-1}, or 4% overall. Figure 7a summarizes the calculated TPB densities for all tested samples. We also compared the fuel cell performance of the Pt/Ru ALD 100 anode, which was the best-performing ALD-treated catalyst, with that of the bare Pt anode over 3 h of operation at 450 °C. We observed very severe degradation in the bare Pt anode, with a performance drop of 2−3 orders of magnitude, and the Pt/Ru ALD 100 treatment effectively minimized degradation, with a performance drop of less than 1 order of magnitude, as shown in Figure 7b.

Bimetallic clusters have been reported to exhibit improved thermal stability compared to pure metal particles,[24,56−59] a phenomenon that can be explained by the nature of the metal−metal interaction. During cell operation, the Ru-coated Pt surface transforms to a Pt/Ru alloy due to increasing bonding energies between the two metals.[58,59] Ru and Pt have melting points of 2250 and 1772 °C, respectively; therefore, the resulting alloy is believed to have a higher melting point than the homogeneous Pt cluster. In addition, Pt and Ru show an electronegativity difference, with values of 2.28 and 2.2, respectively; as such, Ru atoms on the Pt surface readily oxidize, forming a passivated layer and suppressing coarsening of the Pt clusters.[59] Given its unique features, applying ALD to metal cores has therefore been a particularly viable method for stabilizing nanoscale metal catalysts utilized in high temperature applications.[24,56,57]

3.4. Bimetallic Catalyst Effect of ALD Ru. XPS spectra of the sample anodes were acquired after cell operation to further investigate the kinetic effect of ALD Ru coating. No surface etching was applied in order to better identify adsorbates on the catalyst surface; in order to better do so, the C 1s spectra were deconvoluted into C═C, C═O, and COO peaks by Gaussian curve fitting. Figure 8 shows the peak fitting results for the Pt,

DOI: 10.1021/cs502041d
ACS Catal. 2015, 5, 1914−1921

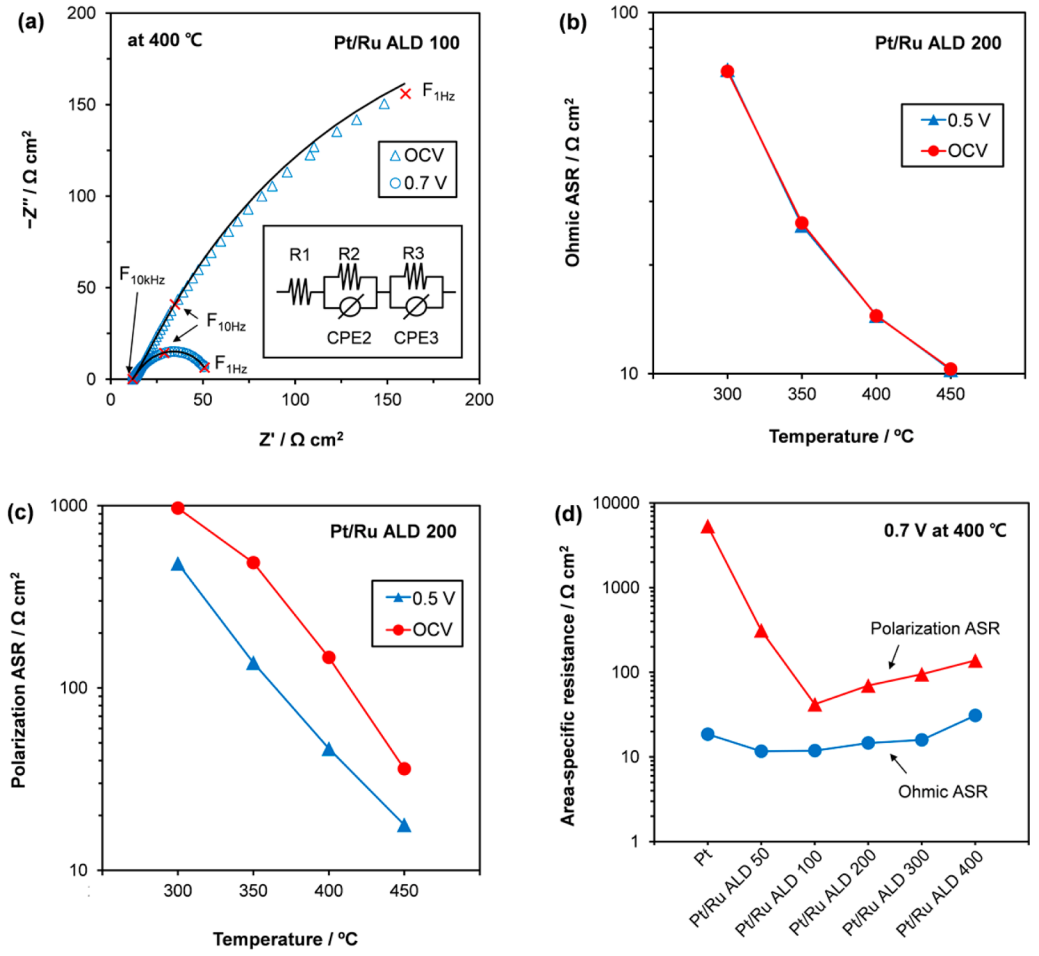

Figure 5. (a) Nyquist impedance spectra of the Pt/Ru ALD 100 cell at 400 °C under both an open circuit bias voltage (OCV) and a 0.7 V cell bias voltage. Electrochemical impedance with respect to (b) ohmic and (c) polarization ASR for the Pt/Ru ALD 200 cell, conducted at OCV and 0.5 V, 300−450 °C. (d) ASR for the Pt, Pt/Ru ALD 50, Pt/Ru ALD 100, Pt/Ru ALD 200, Pt/Ru ALD 300, and Pt/Ru ALD 400 cells, at 0.7 V and 400 °C.

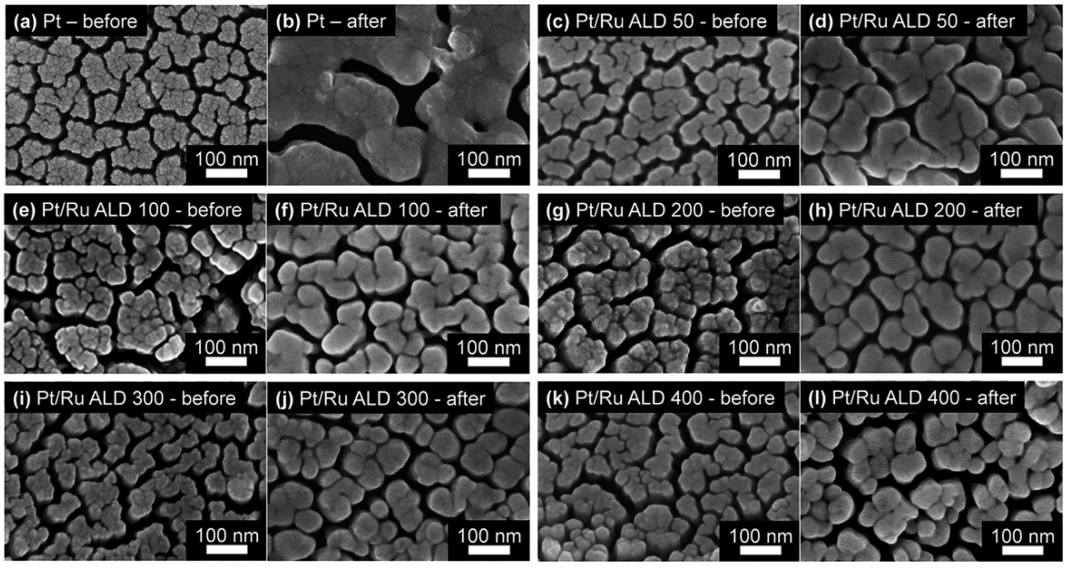

Figure 6. FESEM images of (a)−(b) Pt, (c)−(d) Pt/Ru ALD 50, (e)−(f) Pt/Ru ALD 100, (g)−(h) Pt/Ru ALD 200, (i)−(j) Pt/Ru ALD 300, and (k)−(l) Pt/Ru ALD 400, both before and after cell operation at 450 °C.

Pt/Ru ALD 50, Pt/Ru ALD 100, and Pt/Ru ALD 200 samples. During DMSOFC operation, adsorbed CO groups form either a linear (−CO) or bridge (═CO) bond to Pt, with the former being preferred for high methanol concentrations and the latter

DOI: 10.1021/cs502041d
ACS Catal. 2015, 5, 1914−1921

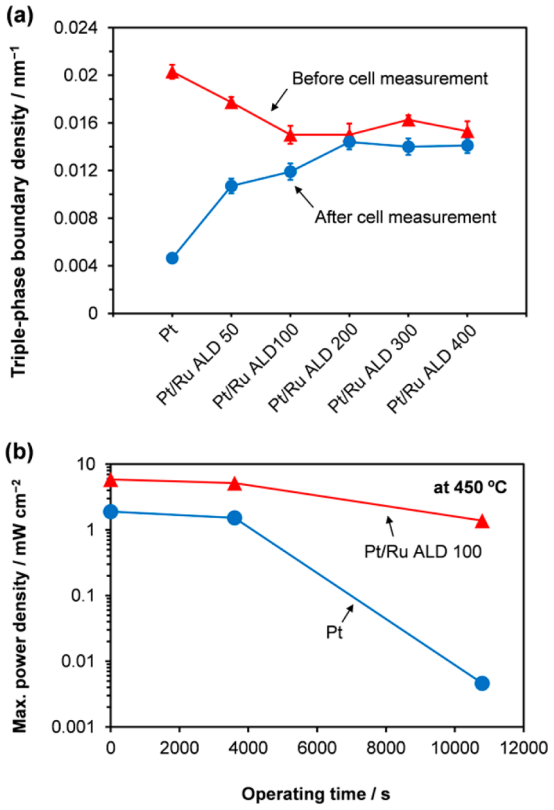

Figure 7. (a) TPB densities for all tested samples both before and after cell operation at 450 °C, based on FESEM images. (b) Comparison of the maximum power densities measured from cells with Pt and Pt/Ru ALD 100 over 3 h of operation at an operating temperature of 450 °C.

being preferred for low.[9,60,61] Figure 9 shows CO anode surface coverage after use for all tested samples. Overall, CO

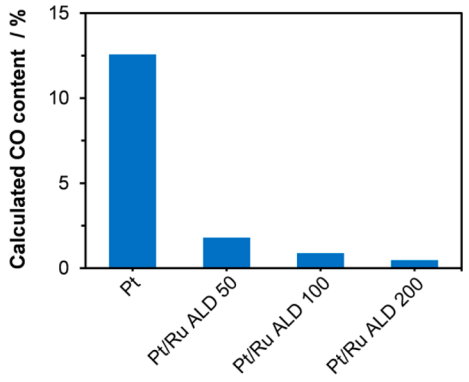

Figure 9. Calculated CO coverage of the used anodes of the Pt, Pt/Ru ALD 50, Pt/Ru ALD 100, and Pt/Ru ALD 200 samples, based on the C 1s XPS spectra.

concentration decreases as Ru content increases, with CO accounting for 12.6% of Pt surface composition versus 0.88% and 0.46% for Pt/Ru ALD 100 and Pt/Ru ALD 200, respectively. This phenomenon can be rationalized by considering the superior ability of Ru to catalyze CO oxidation.[9−11,61] The DMSOFC anode process can be described by the following reaction:

$$CH_3OH + 2O^{2-} \rightarrow CO + 2H_2O + 4e^- \quad (3)$$

Pt is typically considered the best catalysts for this exothermic and thermodynamically favorable reaction.[9−11] Note that adsorbed CO passivates the Pt surface and prevents further methanol oxidation. Removal of these CO groups by oxidation requires the presence of active hydroxyl groups, as shown in the following reaction:

$$CO + OH^- \rightarrow CO_2 + H^+ + 2e^- \quad (4)$$

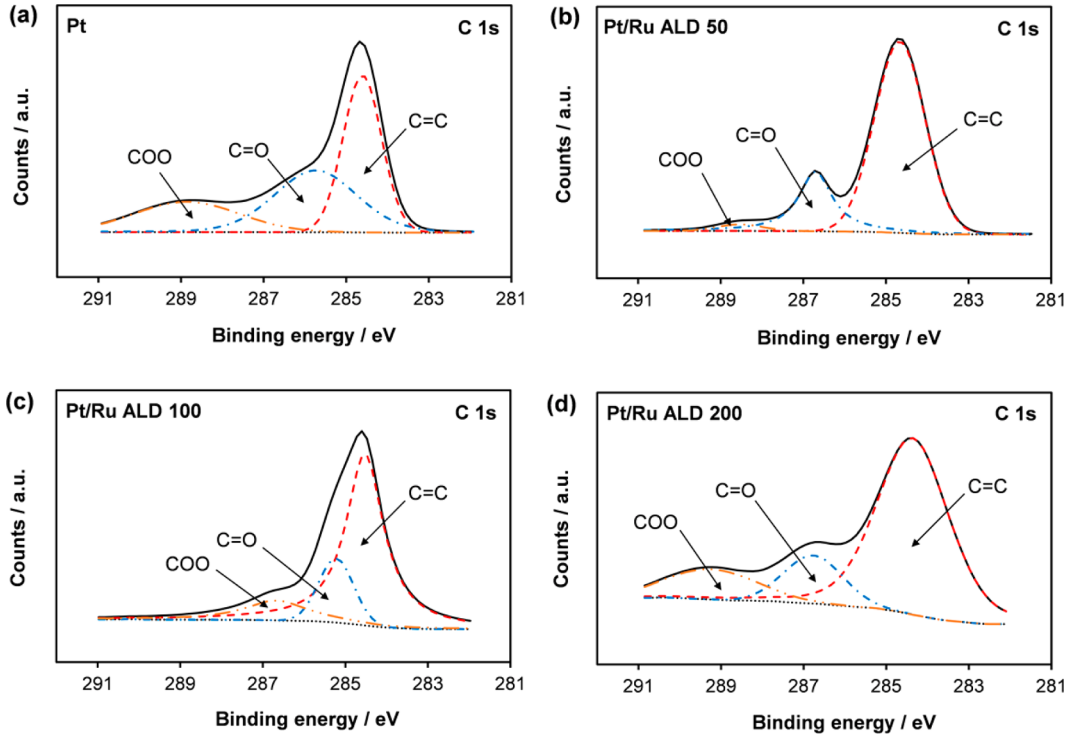

Figure 8. C 1s XPS spectra of the anode surfaces of the (a) Pt, (b) Pt/Ru ALD 50, (c) Pt/Ru ALD 100, and (d) Pt/Ru ALD 200 samples after cell operation at 450 °C, with peak fitting for C═C, C═O, and COO binding spectra.

DOI: 10.1021/cs502041d
ACS Catal. 2015, 5, 1914−1921

Note that the water produced at the anode site can be utilized as a source of OH^- through the following process:

$$H_2O \rightarrow OH^- + H^+ \quad (5)$$

Dehydrogenation of water has been reported as more energetically favorable on Ru than on Pt.[10] Therefore, added Ru should promote OH^- formation, both facilitating CO oxidation and making the Pt surface exclusively available for methanol oxidation. The relatively large anodic overpotential of the Pt and Pt/Ru ALD 50 cells observed through I–V and EIS analysis can therefore be explained by the lack of Ru essential for OH^- generation. In contrast, increased Ru concentration leads to a reduction in the amount of Pt available for methanol oxidation, explaining why the Pt/Ru ALD 200, Pt/Ru ALD 300, and Pt/Ru ALD 400 cells underperform when compared to the Pt/Ru ALD 100 cell.

ALD Ru 200 cycle is more appropriate for Pt electrode stability than ALD Ru 100 cycle. However, ALD Ru 200 cycle covers more Pt electrode essential for dehydrogenation of methanol than ALD Ru 100 cycle, implying catalytically unfavorable for methanol oxidation.

4. CONCLUSIONS

In this study, the DMSOFC electrode performance of Pt catalysts and bimetallic Pt/Ru catalysts prepared by ALD were compared. Ru was deposited by ALD on a sputtered Pt mesh, which was then integrated into a DMSOFC using GDC pellets as the electrolyte. The formation of highly dispersed agglomerations of ALD Ru on the Pt surface was confirmed by HRTEM. Overall, Pt/Ru ALD 100 showed the closest to optimal coverage of ALD Ru, outperforming pure Pt by more than 1 order of magnitude in terms of power output. EIS clearly confirmed that this enhanced cell performance was due to reduced electrode resistance and further showed that the ASR of the Pt/Ru ALD cell was 2 orders of magnitude smaller than that of the pure Pt cell. This technique also helped prevent Pt thermal agglomeration, preserving TPB density and improving operational stability.

XPS confirmed a significant reduction in the amount of postoperational surface-bound CO on the anode, with this effect being more marked for higher Ru coverage. The presence of CO passivates the Pt surface and retards dehydrogenation and methanol oxidation. Therefore, the observed increase in cell performance likely results from improved CO oxidation by ALD Ru. However, Pt-catalyzed methanol oxidation is hindered by excessive Ru coverage, explaining the deterioration in performance observed for the Pt/Ru ALD 200, Pt/Ru ALD 300, and Pt/Ru ALD 400 samples.

■ ASSOCIATED CONTENT

Supporting Information

The following file is available free of charge on the ACS Publications website at DOI: 10.1021/cs502041d.

Supporting figures for Experimental Section and growth mode of Ru fabricated by atomic layer deposition on Pt (PDF)

■ AUTHOR INFORMATION

Corresponding Author

*E-mail: shimm@korea.ac.kr. Tel.: +82-2-3290-3353. Fax: +82-2-926-9290.

Notes

The authors declare no competing financial interest.

■ ACKNOWLEDGMENTS

This work was financially supported by a National Research Foundation of Korea (NRF) Grant funded by the Korean Government (MSIP) (No. NRF-2013R1A1A1A05013794). The Brain Korea 21 Plus program also provided partial support.

■ REFERENCES

(1) Steele, B. C. H.; Heinzel, A. *Nature* **2001**, *414*, 345–352.
(2) Atkinson, A.; Barnett, S.; Gorte, R. J.; Irvine, J. T. S.; McEvoy, A. J.; Mogensen, M.; Singhal, S. C.; Vohs, J. *Nat. Mater.* **2004**, *3*, 17–27.
(3) McIntosh, S.; Gorte, R. J. *Chem. Rev.* **2004**, *104*, 4845–4865.
(4) Liu, M.; Peng, R.; Dong, D.; Gao, J.; Liu, X.; Meng, G. *J. Power Sources* **2008**, *185*, 188–192.
(5) Liu, H.; Song, C.; Zhang, L.; Zhang, J.; Wang, H.; Wilkinson, D. P. *J. Power Sources* **2006**, *155*, 95–110.
(6) Aricò, A. S.; Srinivasan, S.; Antonucci, V. *Fuel cells* **2001**, *1*, 133–161.
(7) Gasteiger, H. A.; Markovic, N.; Ross, P. N., Jr.; Cairns, E. *J. Phys. Chem.* **1993**, *97*, 12020–12029.
(8) Radmilovic, V.; Gasteiger, H. A.; Ross, P. N. *J. Catal.* **1995**, *154*, 98–106.
(9) Hamnett, A. *Catal. Today* **1997**, *38*, 445–457.
(10) Kua, J.; Goddard, W. A. *J. Am. Chem. Soc.* **1999**, *121*, 10928–10941.
(11) Watanabe, M.; Motoo, S. *Electroanal. Chem. Interfacial Electrochem.* **1975**, *60*, 267–273.
(12) Schmidt, T. J.; Noeske, M.; Gasteiger, H. A.; Behm, R. J.; Britz, P.; Brijoux, W.; Bönnemann, H. *Langmuir* **1997**, *13*, 2591–2595.
(13) Takasu, Y.; Fujiwara, T.; Murakami, Y.; Sasaki, K.; Oguri, M.; Asaki, T.; Sugimoto, W. *J. Electrochem. Soc.* **2000**, *147*, 4421–4427.
(14) Paulus, U. A.; Endruschat, U.; Feldmeyer, G. J.; Schmidt, T. J.; Bönnemann, H.; Behm, R. J. *J. Catal.* **2000**, *195*, 383–393.
(15) Steigerwalt, E. S.; Deluga, G. A.; Cliffel, D. E.; Lukehart, C. M. *J. Phys. Chem. B* **2001**, *105*, 8097–8101.
(16) Liu, Z.; Lee, J. Y.; Han, M.; Chen, W.; Gan, L. M. *J. Mater. Chem.* **2002**, *12*, 2453–2458.
(17) Min, Y. S.; Bae, E. J.; Jeong, K. S.; Cho, Y. J.; Lee, J. H.; Choi, W. B.; Park, G. S. *Adv. Mater.* **2003**, *15*, 1019–1022.
(18) Elam, J. W.; Libera, J. A.; Huynh, T. H.; Feng, H.; Pellin, M. J. *J. Phys. Chem. C* **2010**, *114*, 17286–17292.
(19) Shim, J. H.; Kang, S.; Cha, S. W.; Lee, W.; Kim, Y. B.; Park, J. S.; Gür, T. M.; Prinz, F. B.; An, J. *J. Mater. Chem. A* **2013**, *1*, 12695–12705.
(20) George, S. M. *Chem. Rev.* **2010**, *110*, 111–131.
(21) King, J. S.; Wittstock, A.; Biener, J.; Kucheyev, S. O.; Wang, Y. M.; Baumann, T. F.; Giri, S. K.; Hamza, A. V.; Baeumer, M.; Bent, S. F. *Nano Lett.* **2008**, *8*, 2405–2409.
(22) Christensen, S. T.; Elam, J. W.; Rabuffetti, F. A.; Ma, Q.; Weigand, S. J.; Lee, B.; Seifert, S.; Stair, P. C.; Poeppelmeier, K. R.; Hersam, M. C.; Bedzyk, M. J. *Small* **2009**, *5*, 750–757.
(23) Liu, C.; Wang, C. C.; Kei, C. C.; Hsueh, Y. C.; Perng, T. P. *Small* **2009**, *5*, 1535–1538.
(24) Shim, J. H.; Jiang, X.; Bent, S. F.; Prinz, F. B. *J. Electrochem. Soc.* **2010**, *157*, B793–B797.
(25) Christensen, S. T.; Feng, H.; Libera, J. L.; Guo, N.; Miller, J. T.; Stair, P. C.; Elam, J. W. *Nano Lett.* **2010**, *10*, 3047–3051.
(26) Feng, H.; Elam, J. W.; Libera, J. A.; Setthapun, W.; Stair, P. C. *Chem. Mater.* **2010**, *22*, 3133–3142.
(27) Feng, H.; Libera, J. A.; Stair, P. C.; Miller, J. T.; Elam, J. W. *ACS Catal.* **2011**, *1*, 665–673.
(28) Enterkin, J. A.; Poeppelmeier, K. R.; Marks, L. D. *Nano Lett.* **2011**, *11*, 993–997.
(29) Enterkin, J. A.; Setthapun, W.; Elam, J. W.; Christensen, S. T.; Rabuffetti, F. A.; Marks, L. D.; Stair, P. C.; Poeppelmeier, K. R.; Marshall, C. L. *ACS Catal.* **2011**, *1*, 629–635.

DOI: 10.1021/cs502041d
ACS Catal. 2015, 5, 1914–1921

(30) Marichy, C.; Bechelany, M.; Pinna, N. *Adv. Mater.* **2012**, *24*, 1017−1032.
(31) Jiang, X.; Gür, T. M.; Prinz, F. B.; Bent, S. F. *Chem. Mater.* **2010**, *22*, 3024−3032.
(32) An, J.; Kim, Y. B.; Prinz, F. B. *Phys. Chem. Chem. Phys.* **2013**, *15*, 7520−7525.
(33) Aaltonen, T.; Alén, P.; Ritala, M.; Leskelä, M. *Chem. Vap. Deposition* **2003**, *9*, 45−49.
(34) Alayoglu, S.; Nilekar, A. U.; Mavrikakis, M.; Eichhorn, B. *Nat. Mater.* **2008**, *7*, 333−338.
(35) Lewera, A.; Zhou, W. P.; Vericat, C.; Chung, J. H.; Haasch, R.; Wieckowski, A.; Bagus, P. S. *Electrochim. Acta* **2006**, *51*, 3950−3956.
(36) Jung, D. W.; Duncan, K. L.; Wachsman, E. D. *Acta Mater.* **2010**, *58*, 355−363.
(37) Wachsman, E. D.; Lee, K. T. *Science* **2011**, *334*, 935−939.
(38) Son, K. S.; Bae, K.; Kim, J. W.; Ha, J. S.; Shim, J. H. *J. Vac. Sci. Technol., A* **2013**, *31*, 01A107−1−01A107−4.
(39) Choi, H. J.; Park, S. W.; Han, G. D.; Na, J.; Kim, G. T.; Shim, J. H. *Appl. Phys. Lett.* **2014**, *104*, 242105−1−242105−4.
(40) Aaltonen, T.; Rahtu, A.; Ritala, M.; Leskelä, M. *Solid-State Lett.* **2003**, *6*, C130−C133.
(41) Kwon, O. K.; Kim, J. H.; Park, H. S.; Kang, S. W. *J. Electrochem. Soc.* **2004**, *151*, G109−G112.
(42) Anderson, V. R.; Leick, N.; Clancey, J. W.; Hurst, K. E.; Jones, K. M.; Dillon, A. C.; George, S. *J. Phys. Chem. C* **2014**, *118*, 8960−8970.
(43) Park, K. J.; Doub, J. M.; Gougousi, T.; Parsons, G. N. *Appl. Phys. Lett.* **2005**, *86*, 051903−1−051903−3.
(44) Johansson, A. C.; Larsen, J. V.; Verheijen, M. A.; Haugshøj, K. B.; Clausen, H. F.; Kessels, W. M. M.; Christensen, L. H.; Thomsen, E. V. *J. Catal.* **2014**, *311*, 481−486.
(45) Vitos, L.; Ruban, A. V.; Skriver, H. L.; Kollar, J. *Surf. Sci.* **1998**, *411*, 186−202.
(46) Farmer, D. B.; Gordon, R. G. *Nano Lett.* **2006**, *6*, 699−703.
(47) Wu, Y. Q.; Ye, P. D.; Capano, M. A.; Xuan, Y.; Sui, Y.; Qi, M.; Cooper, J. A.; Shen, T.; Pandey, D.; Prakash, G.; Reifenberger, R. *Appl. Phys. Lett.* **2008**, *92*, 092102−1−092102−3.
(48) Park, S. W.; Kim, J. W.; Choi, H. J.; Shim, J. H. *J. Vac. Sci. Technol., A* **2014**, *32*, 01A115−1−01A115−5.
(49) Venables, J. A.; Spiller, G. D. T.; Hanbucken, M. *Rep. Prog. Phys.* **1984**, *47*, 399−459.
(50) Markov, I. V. *Crystal Growth for Beginners: Fundamentals of Nucleation, Crystal Growth, and Epitaxy*; World Scientific: Singapore, 1995; pp 375−406.
(51) O'Hayre, R. P.; Cha, S. W.; Colella, W. G.; Prinz, F. B. *Fuel Cell Fundamentals*, 2nd ed.; Wiley: New York, 2009; pp 234−250.
(52) Kim, Y. B.; Shim, J. H.; Gür, T. M.; Prinz, F. B. *J. Electrochem. Soc.* **2011**, *158*, B1453−B1457.
(53) Chao, C. C.; Motoyama, M.; Prinz, F. B. *Adv. Energy Mater.* **2012**, *2*, 651−654.
(54) Wang, X.; Huang, H.; Holme, T.; Tian, X.; Prinz, F. B. *J. Power Sources* **2008**, *175*, 75−81.
(55) Takagi, Y.; Lai, B. K.; Kerman, K.; Ramanathan, S. *Energy Environ. Sci.* **2011**, *4*, 3473−3478.
(56) Biener, M. M.; Biener, J.; Wichmann, A.; Wittstock, A.; Baumann, T. F.; Bäumer, M.; Hamza, A. V. *Nano Lett.* **2011**, *11*, 3085−3090.
(57) Lu, J.; Fu, B.; Kung, M. C.; Xiao, G.; Elam, J. W.; Kung, H. H.; Stair, P. C. *Science* **2012**, *335*, 1205−1208.
(58) Cheng, D.; Huang, S.; Wang, W. *Phys. Rev. B* **2006**, *74*, 064117−1−064117−11.
(59) Liu, X.; Wang, A.; Yang, X.; Zhang, T.; Mou, C. Y.; Su, D. S.; Li, J. *Chem. Mater.* **2009**, *21*, 410−418.
(60) Wilhelm, S.; Iwasita, T.; Vielstich, W. *J. Electroanal. Chem. Interfacial Electrochem.* **1987**, *238*, 383−391.
(61) Iwasita, T. *Electrochim. Acta* **2002**, *47*, 3663−3674.

DOI: 10.1021/cs502041d
ACS Catal. 2015, 5, 1914−1921